

## Determination of an Amazon Hot Reference Target for the On-Orbit Calibration of Microwave Radiometers

SHANNON T. BROWN AND CHRISTOPHER S. RUF

*Department of Atmospheric, Oceanic and Space Sciences, University of Michigan, Ann Arbor, Michigan*

(Manuscript received 12 May 2004, in final form 14 January 2005)

### ABSTRACT

A physically based model is developed to determine hot calibration reference brightness temperatures ( $T_{BS}$ ) over depolarized regions in the Amazon rain forest. The model can be used to evaluate the end-to-end calibration of any satellite microwave radiometer operating at a frequency between 18 and 40 GHz and angle of incidence between nadir and  $55^\circ$ . The model is constrained by Special Sensor Microwave Imager (SSM/I)  $T_{BS}$  measured at 19.35, 22.2, and 37.0 GHz at a  $53^\circ$  angle of incidence and extrapolates/interpolates those measurements to other frequencies and incidence angles. The rms uncertainty in the physically based model is estimated to be 0.57 K. For instances in which coincident SSM/I measurements are not available, an empirical formula has been fit to the physical model to provide hot reference brightness temperature as a function of frequency, incidence angle, time of day, and day of year. The empirical formula has a 0.1-K rms deviation from the physically based model for annual averaged measurements and at most a 0.6-K deviation from the model for any specific time of day or day of year.

### 1. Introduction

Satellite microwave radiometers have provided measurements from space of atmospheric constituents, near-surface winds, ocean surface roughness, sea ice concentration, land surface vegetation and soil moisture content, and other geophysical parameters for more than 30 years (e.g., Ulaby et al. 1986; Grody 1993). Microwave radiometers typically measure the brightness temperature of a scene at a number of frequencies in order to distinguish the various geophysical contributors according to their distinct emission spectra (e.g., Keihm et al. 1995). The accuracy of such an inversion procedure is critically dependent on the calibration of the measurements. The brightness temperature is calibrated in a two-stage process. Raw receiver voltage counts are converted to the antenna-beam-averaged temperature ( $T_A$ ) by an antenna temperature calibration algorithm (e.g., Ruf et al. 1995). The  $T_A$  is converted to the main-beam-referenced brightness temperature ( $T_B$ ) by an antenna pattern correction (APC) algorithm (e.g., Janssen et al. 1995). A number

of calibration coefficients are associated with both the antenna temperature and APC algorithms. They are estimated prior to launch using a combination of laboratory, antenna range, and thermal/vacuum chamber measurements together with computer models. Some of the coefficients are often further adjusted after launch as part of the early calibration/validation phase of a mission.

Antenna temperature calibration relies on observations of hot and cold reference targets. For most satellite radiometers, the electrical path from the reference targets to the receiver is not identical to the electrical path from the earth observing antenna to the receiver. Compensation for these differences requires a model for signal propagation. Parameters of that model can be adjusted on orbit. Reasons that the prelaunch values may be inaccurate can include significant differences between the thermal environment experienced in space and while testing before flight, as well as hardware changes that may occur during launch. The APC algorithm compensates for the sensitivity of a radiometer's measurements to incident radiation from all directions, weighted by its antenna directivity pattern. The algorithm needs to remove contributions to the measurements from radiation entering the antenna sidelobes, most importantly the sidelobes that view cold space,

---

*Corresponding author address:* Chris Ruf, University of Michigan, 2455 Hayward St., Ann Arbor, MI 48109-2143.  
E-mail: cruf@umich.edu

and it needs to rescale the remaining contributions—those entering the antenna main beam—to the level that would have been measured had the sidelobes not been present. In both cases, the proper correction requires accurate knowledge of the directive characteristics of the antenna. Integrated directivities over the appropriate main beam and sidelobe solid angles produce calibration coefficients that are used in the correction algorithm. These coefficients may need to be adjusted on orbit, primarily because low-level sidelobes are extremely difficult to measure accurately without an exact replica of the entire spacecraft being present during the measurement. This is in most cases impractical. As a general rule, coefficients in the APC algorithm are more prone to need of adjustment on orbit compared to hardware thermal loss coefficients due to the larger uncertainties in their prelaunch measurement.

On orbit calibration of a radiometer is ideally an “end-to-end” procedure in which known values of the  $T_B$  in the antenna main beam are observed and compared to the calibrated data (e.g., Ruf et al. 1994). Such a test verifies the entire chain of calibration algorithms as well as all components of the hardware. It is best to perform such a test over the full dynamic range of the instrument. The dynamic range of  $T_B$ s that an earth observing radiometer will encounter is approximately 120–310 K over the range 18–40 GHz and 0°–55° incidence for either vertical or horizontal linear polarization. A method developed by Ruf (2000), which isolates a statistical lower bound on brightness temperature over the ocean, can be used to calibrate the  $T_B$  at the cold end of the range. There remains a need for a reliable on-earth hot calibration reference target. An ideal target would be a large isothermal blackbody extending over the main beam of the earth-pointing antenna. Heavily vegetated regions of the Amazon rain forest can provide a viable approximation to a blackbody target. The regions have certain radiative properties in the microwave—discussed in detail below—which make them especially amenable to use as hot reference targets. Taken together, the minimum ocean and hot Amazon  $T_B$ s provide reference calibration targets at the high and low end of a radiometer’s dynamic range that can be used to verify (and correct if necessary) the end-to-end calibration accuracy of a spaceborne microwave radiometer.

This paper presents two parameterized models for an Amazon hot calibration reference target. They have both been tuned to specific, optimal regions of the Amazon rain forest. Both models are physically derived and tuned to measurements made by the Defense Meteorological Satellite Program (DMSP) Special Sensor Microwave Imager (SSM/I). For this reason, the models

should be considered as a method for transferring the calibration accuracy of SSM/I to other instruments. SSM/I calibration performance has been extensively evaluated and is widely regarded as extremely stable over time and between different units on orbit (Colton and Poe 1999). However, it should be noted that the detailed quantitative behavior of our results is ultimately dependent on the accuracy of SSM/I calibration. The models are adjustable in frequency over the range from 18 to 40 GHz and in incidence angle over the range from nadir to 55°. The specific Amazon regions that have been selected are effectively unpolarized, so these models can be used for any linear or circular polarized channel. The first of the two models is intended for investigations in which SSM/I measurements of the Amazon regions are available that are roughly coincident in time with those of another radiometer under test. The model parameterizes the extrapolation from SSM/I  $T_B$  measurements—at SSM/I frequencies and incidence angle—to the  $T_B$ s that would have been observed at other frequencies and incidence angles. This is the more accurate of the two models. The second model further parameterizes the dependence of SSM/I observations on local time of day and month of the year. It is intended for investigations for which coincident SSM/I observations are not available. Parameterization of these time dependences introduces at most a 0.6-K rms error into the second model.

Section 3 of this paper describes the development of the Amazon hot reference model. Included are descriptions of the underlying physical model, the method for identifying suitable regions of the Amazon, and details concerning the parameterization of the atmospheric component of the model. The section concludes with a description of the method by which SSM/I observations are used to “train” the parameters of the model. Section 4 describes various characteristics of the model, including its behavior with respect to frequency, angle of incidence, local time of day, and month of the year. Section 5 gives examples of how the models should be used in cases when coincident SSM/I observations either are or are not available. Section 6 presents conclusions and discussion.

## 2. Description of SSM/I dataset

The measured  $T_B$  dataset consists of measurements from October 2001 through September 2002 from the DMSP SSM/I *F13*, *F14*, and *F15* platforms acquired from Remote Sensing Systems. SSM/I is a conically scanning multichannel dual-polarization radiometer at an incidence of 53°. It has vertically and horizontally polarized 19.35-, 37.0-, and 85.0-GHz channels, as well as a vertically polarized 22.235-GHz channel. Each

platform is in a near-polar sun-synchronous orbit. The local equator crossing times are 0615 and 1815 local solar time (LST) for F13, 0821 and 2021 LST for F14, and 0931 and 2131 LST for F15. This gives a good representation of morning, afternoon, and evening data.

The SSM/I  $T_B$ s were determined from the antenna temperatures ( $T_A$ s) using the antenna pattern correction (APC) algorithm described in Wentz (1991). The APC algorithm corrects for cross-polarization contamination, although this will be a small correction term over the nearly depolarized Amazon regions, and the feed horn spillover, which is a large correction term due to the contrast between the earth scene ( $\sim 280$  K) and cold space (2.7 K). The  $T_B$  is approximately 9 K higher than the  $T_A$  at 19.35 GHz, 7.5 K higher at 22.235 GHz, and 4 K higher at 37.0 GHz. A single set of APC coefficients is used for all platforms to minimize intersensor differences, as recommended by Colton and Poe (1999). These coefficients can be found in Wentz (1991). Only SSM/I data from scan position 10 to 40 was used because of calibration offsets at higher scan positions caused by the feed horn partially viewing the cold-space reflector.

The  $T_B$  dataset is filtered for rain by removing data for which the difference between the 19.35- and 37.0-GHz V-pol  $T_B$ s is greater than 4.5 K. This is the maximum difference found using the radiative transfer model on rain-free atmospheres. The difference would become larger in the presence of rain due to increased absorption (higher in the atmosphere) and scattering at 37.0 GHz relative to 19.35 GHz. To ensure the validity of the surface emission model and to aid in the convergence of the iterative technique, the 19.35- and 37.0-GHz V-pol minus H-pol  $T_B$  difference was required to be less than 3 K and greater than 0 K. In practice, very few data points laid outside these limits.

### 3. Development of the Amazon hot reference model

#### a. Physical model

The surface brightness temperature of a weakly scattering canopy over a semi-infinite soil layer can be modeled as (Ulaby et al. 1982)

$$T_{B\text{canopy}}(f, \theta, p) = \left(1 + \frac{\Gamma_s(f, \theta, p)}{L(f, \theta)}\right) \left(1 - \frac{1}{L(f, \theta)}\right) \times [1 - a(f)]T_v + \left(\frac{1 - \Gamma_s(f, \theta, p)}{L(f, \theta)}\right)T_s, \quad (1)$$

where  $\theta$  is incidence angle,  $f$  is frequency,  $p$  is polarization,  $\Gamma_s(f, \theta, p)$  is soil-vegetation reflectivity,  $L(f, \theta)$  is

loss factor of the vegetation canopy ( $=e^{\tau_{\text{canopy}} \sec\theta}$ ),  $a(f)$  is single scattering albedo of the canopy,  $T_v$  is physical temperature of the canopy, and  $T_s$  is physical temperature of the surface. At frequencies greater than 10 GHz with a dense canopy, the optical depth of the vegetation becomes very large and the transmissivity of the canopy (inverse of the loss factor) approaches zero. In this case, the brightness temperature of the canopy reduces to

$$T_{B\text{canopy}} = [1 - a(f)]T_v, \quad (2)$$

where the surface scattering is assumed to be isotropic. It is reasonable to assume that there is a variation of the single scattering albedo with frequency since the wavelength of the radiation changes relative to the leaf dimensions of the vegetation. According to Eq. (2), the  $T_B$  of the canopy has no dependence on incidence angle or polarization. Using this model for the surface emission, the theoretical brightness temperature observed by a satellite radiometer over a canopy can be found at any frequency and incidence angle, provided the surface temperature, single scattering albedo, atmospheric integrated optical depth, and atmospheric upwelling and downwelling  $T_B$ s are known at the frequency of interest. These variables can be estimated using an atmospheric model and SSM/I multifrequency brightness temperature observations.

The integrated optical depth of the atmosphere can be linearly related to the absorbing components of the atmosphere by

$$\tau(f) = b_0(f) + b_1(f)A, \quad (3)$$

where  $\tau$  is the integrated optical depth,  $A$  is a function of the integrated water vapor content and the cloud liquid water content of the atmosphere, and  $b_{0,1}(f)$  are frequency dependent coefficients to be determined. The optical depth has been limited to one degree of freedom since there are not enough constraints to independently retrieve the cloud liquid and water vapor concentrations as well as the surface parameters. The rms difference between Eq. (3) and the true optical depth increases by 2.9% for 37.0 GHz, 0.4% for 22.235 GHz, and negligibly for 19.35 GHz compared to using a two-parameter equation of the form  $[b_0(f) + b_1(f)V + b_2(f)L]$ . Assuming a horizontally uniform and azimuthally symmetric atmosphere, the upwelling and downwelling  $T_B$ s can be related to the integrated optical depth using an effective radiating temperature of the atmosphere, as

$$T_B^{\text{UP}}(f, \theta) = T_{\text{eff}}^{\text{UP}}(f)(1 - e^{-\tau(f) \sec\theta}) \quad (4a)$$

$$T_B^{\text{DN}}(f, \theta) = T_{\text{eff}}^{\text{DN}}(f)(1 - e^{-\tau(f) \sec\theta}) + T_{\text{cosmic}}e^{-\tau(f) \sec\theta}, \quad (4b)$$

where  $T_B^{\text{UP}}$  and  $T_B^{\text{DN}}$  are the upwelling and downwelling  $T_B$ s;  $T_{\text{eff}}^{\text{UP}}$  and  $T_{\text{eff}}^{\text{DN}}$  are the upwelling and downwelling atmospheric effective radiating temperatures, which are determined from a radiative transfer model; and  $T_{\text{cosmic}}$  is the microwave cosmic background temperature. This type of atmospheric model has been used in other radiometric surface parameter retrievals (Wilheit and Fowler 1977; Piepmeier and Gasiewski 2001).

The single scattering albedo is assumed to be linearly related to frequency by

$$a(f) = d_0 + d_1 f, \quad (5)$$

where  $f$  is in gigahertz and the  $d_{0,1}$  coefficients are to be determined. The use of this simplified parametric model for the canopy emission over 18–40 GHz is justified by both models and observations. Isaacs et al. (1989) developed a model for the emissivity of a heavily vegetated scene based on radiative transfer through a continuous random media and determined that, for optically thick (i.e., water laden) vegetation, the emissivity increased with frequency at frequencies less 10 GHz and then monotonically decreased with frequency at frequencies greater than 10 GHz. This behavior results because, once the optical depth of the canopy becomes large enough to obscure emission from the surface (which occurs near 10 GHz for a thick canopy), any further increase in frequency tends to increase the scattering by the canopy, which will lower the effective emissivity of the surface plus canopy. Above 10 GHz, the emissivity modeled by Isaacs et al. (1989) was also unpolarized and had little angular dependence. A more recent model for the emissivity of a leafy deciduous forest also showed saturation effects at 10 GHz for high biomass content (Ferrazzoli and Guerriero 1996). Satellite observations from SSM/I have been used to estimate the emissivity over tropical rain forests and show a monotonic decrease in the emissivity from 19 to 37 GHz (Hiltbrunner et al. 1994; Prigent et al. 1997). Aircraft observations of summertime deciduous forests in Italy also show a decrease in emissivity from 10 to 37 GHz (Macelloni et al. 2001).

The  $T_B$  observed by a satellite radiometer as a function of frequency and incidence angle is then given by the radiative transfer equation

$$T_B(f, \theta) = (1 - a(f))T_v e^{-\tau(f) \sec \theta} + T_B^{\text{UP}}(f, \theta) + \frac{a(f)}{2} \times \left[ \frac{1}{2\pi} \int_{2\pi} T_B^{\text{DN}}(f, \Omega') \cos \theta' d\Omega' \right] e^{-\tau(f) \sec \theta}, \quad (6)$$

where the last term on the right is the hemispherically integrated downwelling  $T_B$  that is scattered isotropically by the canopy and observed in the direction of incidence. The factor of  $1/2$  is present in the last term because we are only concerned with the radiation scattered back into the upper hemisphere. To solve for  $T_B(f, \theta)$ , we first parameterize the atmospheric model using a radiative transfer model, then solve for  $T_v$ ,  $d_0$ ,  $d_1$ , and  $A$  over suitable regions using SSM/I  $T_B$  observations at three frequencies and a nonlinear optimal estimation method.

### b. Selecting suitable regions of the Amazon rain forest

For Eq. (2) to be valid, the emission from the canopy must be independent of incidence angle and polarization. The second requirement is used to find suitable heavily vegetated regions in the Amazon rain forest. In general, the polarization dependence of vegetated land surfaces at oblique observing angles comes primarily from the underlying soil emission. In the Amazon, the vegetation canopy can at times be dense, water laden, and optically thick. The polarization dependence will tend to decrease as the optical depth increases and the surface is obscured. In the limit as the polarization dependence vanishes, the canopy becomes opaque. The loss factor of the canopy [ $L$  in Eq. (1)] will still scale with pathlength between nadir and  $53^\circ$ , but there is no effect on canopy brightness as  $L \rightarrow \infty$ . This means that the depolarized regions should also have little angular dependence. The regions were selected based on the magnitude of the vertically and horizontally polarized  $T_B$  difference as measured by the SSM/I radiometer at its two window channels of 19.35 and 37.0 GHz. Two regions were selected where the mean polarization difference was less than 0.75 K. The selection criterion locates regions with an optically thick vegetation canopy where the emission is independent of incidence angle and polarization. The selected regions were made as large as possible in order to accommodate as wide a variety as possible of radiometers under test, with regard to antenna beamwidths, scanning geometries, and earth coverage. Region 1 is bounded by  $5^\circ$ – $10^\circ$ S and  $65^\circ$ – $74^\circ$ W, and region 2 is bounded by  $1^\circ$ S– $4^\circ$ N and  $53^\circ$ – $59^\circ$ W. Table 1 shows the value of the vertically and horizontally polarized  $T_B$  difference averaged over the regions at both 19.35 and 37.0 GHz. An image of the 37.0-GHz  $|V\text{-pol} - H\text{-pol}| T_B$ s over the Amazon basin with the regions highlighted is shown in Fig. 1. The Amazon River and its tributaries are clearly visible, as well as deforested civilized areas.

TABLE 1. Statistics of the second Stokes parameter from SSM/I data (Jan–Sep 2002).

$T_B(V\text{-pol}) - T_B(H\text{-pol})$	Region 1 (5°–10°S, 65°–74°W)	Region 2 (1°S–4°N, 53°–59°W)
19.35 GHz	Mean: 0.75 K Std dev: 0.84 K	Mean: 0.55 K Std dev: 0.81 K
37.0 GHz	Mean: 0.74 K Std Dev: 0.78 K	Mean: 0.53 K Std dev: 0.67 K

*c. Parameterization of the atmospheric component of the model*

The  $b$  coefficients in Eq. (3) and the effective radiating temperatures in Eqs. (4a) and (4b) must be determined using a radiative transfer model. These coefficients and radiating temperatures are determined at SSM/I frequencies and at 500-MHz intervals between 18 and 40 GHz. A plane parallel radiative transfer model is used with radiosonde profiles (raobs) from launch sites in the vicinity of the selected regions in order to estimate the integrated atmospheric optical depth and the upwelling and downwelling  $T_{BS}$ . The atmospheric gaseous absorption is determined using the

Rosenkranz (1993) oxygen absorption model and an updated version of the Liebe water vapor absorption model (Cruz-Pol et al. 1998). A model from Walcek and Taylor (1986) is used to estimate the amount of cloud liquid water present in each radiosonde profile. The cloud liquid water absorption model is from Benoit (1968). The atmospheric absorption parameter,  $A$  in Eq. (3), is given by

$$A = V + 2L, \quad (7)$$

where  $V$  is the integrated water vapor content (cm) and  $L$  is the cloud liquid water content (mm). This function provides an excellent fit between the integrated optical depth and the absorption components  $V$  and  $L$ . A regression between  $A$  and the calculated optical depth at each frequency is used to determine the  $b$  coefficients in Eq. (3). The upwelling and downwelling effective radiating temperatures (shown in Fig. 2) are determined using Eqs. (4a) and (4b) together with the atmospheric upwelling and downwelling  $T_{BS}$  and optical depth determined from the radiative transfer model and are taken to be the average over the entire model dataset.

Raob sounding data from October 2001 through September 2002, corresponding with the dates of the SSM/I

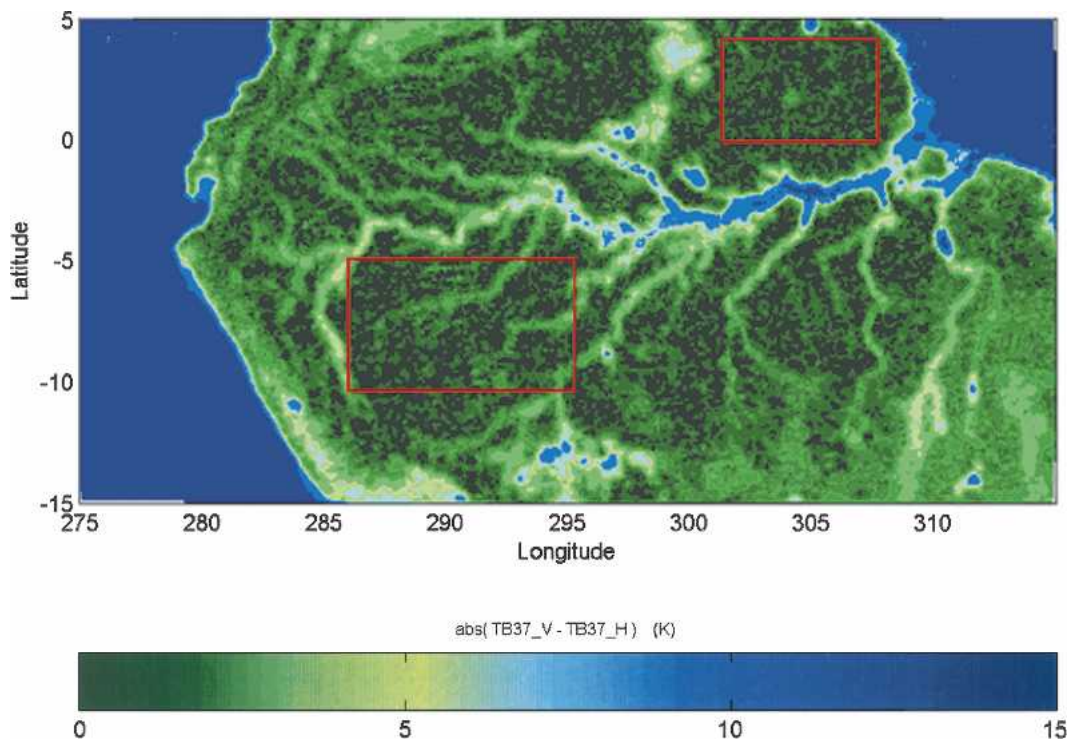


FIG. 1. Magnitude of the difference between vertically and horizontally polarized brightness temperature at 37 GHz, 53° incidence angle over the Amazon basin as measured by SSM/I. The red boxes denote regions of high depolarization, which have properties especially amenable to modeling as blackbody hot calibration reference sites.

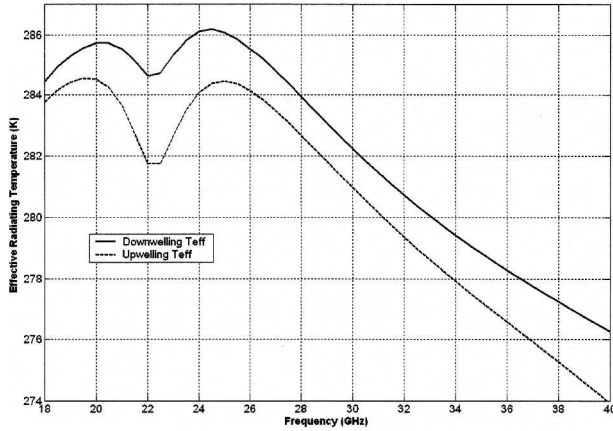


FIG. 2. Effective radiating temperature of the atmosphere vs frequency for upwelling and downwelling emission, derived from radiosonde profiles in the Amazon. Higher downwelling  $T_{\text{eff}}$  results from the air temperature profile. Lower  $T_{\text{eff}}$  in the vicinity of the water vapor line at 22.2 GHz results from pressure broadened increase in attenuation/emission with altitude.

dataset, are used in the model. Four raob stations, located in the Amazon basin, were used (see Table 2). The radiosonde data were acquired from the NOAA Forecast Systems Laboratory (FSL) radiosonde database.

*d. Using SSM/I observations to train the parameters of the model*

The Amazon hot reference  $T_B$  at any frequency and incidence angle (18–40 GHz,  $0^\circ$ – $55^\circ$ ) can be found using Eq. (6) and the parameterized atmospheric model, provided that the absorption parameter  $A$ , the surface temperature  $T_v$ , and the coefficients  $d_0$  and  $d_1$  in Eq. (5) are known. These variables are determined from the parameterized atmospheric model together with SSM/I  $T_B$  measurements at 19.35, 22.235, and 37.0 GHz over the two Amazon regions using a nonlinear iterative optimal estimation technique.

For each SSM/I observation at 19.35, 22.235, and 37.0 GHz, the values of  $A$ ,  $T_v$ ,  $d_0$ , and  $d_1$  are determined using a multivariate iterative Gauss–Newton technique that minimizes the rms difference between the modeled

and measured  $T_B$ s at the three frequencies. Values in the associated Jacobian matrix were determined numerically. Since there are more unknowns than constraints, multiple (nonunique) solutions result. A priori bounds on the variables were used to select a solution by applying a penalty to the minimized cost function for straying far from the a priori mean of each variable. This reduces the dimensionality of the problem from four to three unknowns:  $(d_0T_v)$ ,  $(d_1T_v)$ , and  $A$ . The average of the  $V$ -pol and  $H$ -pol  $T_B$ s at 19.35 and 37.0 GHz were used in the inversion. Given the values of  $A$ ,  $T_v$ ,  $d_0$ , and  $d_1$ , the parameterized atmospheric model was used with Eq. (6) to determine a theoretical brightness temperature at 500-MHz intervals between 18 and 40 GHz and at  $13.5^\circ$  intervals of incidence angle between  $0^\circ$  and  $55^\circ$ . The calculated theoretical brightness temperatures were then averaged by local time and month, giving a four-dimensional matrix of theoretical  $T_B$ s as a function of frequency, incidence angle, time of day, and time of year.

**4. Behavior of the Amazon hot reference temperatures**

The Amazon hot reference temperatures for the two regions are a function of frequency, incidence angle, time of day, and time of year. The reference temperature generally decreases from 18 to 40 GHz, with a small depression around the 22.235-GHz water vapor line. The higher frequencies have a lower reference temperature due to increased absorption by atmospheric oxygen and increasing single scattering albedo, which will tend to lower the upwelling contribution from the surface. The depression around the water vapor line is not very large because the bulk of the water vapor is close to the surface, whereas oxygen is well mixed in the atmosphere. The reference temperature decreases slightly with increasing incidence angle, which is due to the larger optical path through the atmosphere. The decrease in reference temperature with incidence angle is maximum around the water vapor line, owing to a larger contribution from water vapor higher in the atmosphere. The annually and daily averaged reference temperatures as a function of frequency and incidence angle for regions 1 and 2 are shown in Fig. 3.

There are also trends with time of day and time of year. On the annual average, the reference temperature at a certain frequency and incidence is lowest at 0600 LST and warmest at 1000 LST. This difference is approximately 5.5 K at nadir. The 0800, 2000, and 2100 LST reference temperatures have very similar magnitudes on the annual average. The 2200 LST tempera-

TABLE 2. Raob launching stations in the vicinity of the selected blackbody regions.

Station name	WMO		
	ID	Latitude	Longitude
Leticia/Vasquez Cobo (SKLT)	80398	4.17°S	69.95°W
Cayenne/Rochambeau (SOCA)	81405	4.83°N	52.37°W
Manaus/Ponta Pelada (SBMN)	82332	3.15°S	59.98°W
Alta Floresta (SBAT)	82965	9.87°S	56.10°W

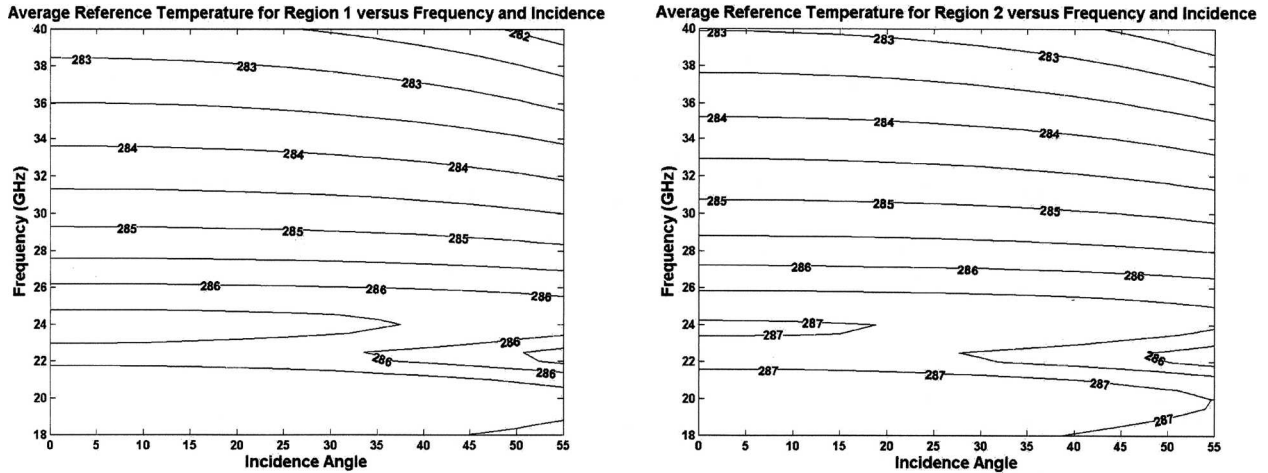


FIG. 3. Average Amazon hot reference temperature as a function of frequency and incidence angle, averaged annually and daily for (left) region 1 and (right) region 2.

ture is greater than at 0600 LST but less than at 0800 LST. The decrease in reference temperature with incidence angle is greatest at 1000 LST and is almost negligible, away from the water vapor line, at 0600 LST. This is because at 0600 LST, the atmosphere is stable on average with most of the water vapor near the surface. A few hours after sunrise, vertical mixing occurs in the boundary layer, increasing the height of the water vapor column, thus decreasing the brightness temperature at higher incidence angles. The dependence of reference temperature with local time is shown in Fig. 4.

The Amazon has two seasons, a wet (rainy) season and a “dry” (less rainy) season. The wet season is approximately from December to May and the dry season from June through November. The surface tempera-

ture is fairly constant year-round, with an annual variation of less than 2 K peak to peak. A plot of the climatological surface temperature from several observing stations in regions 1 and 2 is shown in Fig. 5. This data was acquired from the National Climatic Data Center. The hot reference  $T_B$  also show little annual variation. On a daily average, the reference temperature does not change much throughout the year at any given frequency and incidence angle. Figure 6 shows the reference temperature versus frequency at nadir incidence for selected months. The daily average is warmest during October and coolest in July. This difference is approximately 2.5 K at nadir, which is less than half of the diurnal variation. The seasonal variation is relatively independent of incidence angle except around the wa-

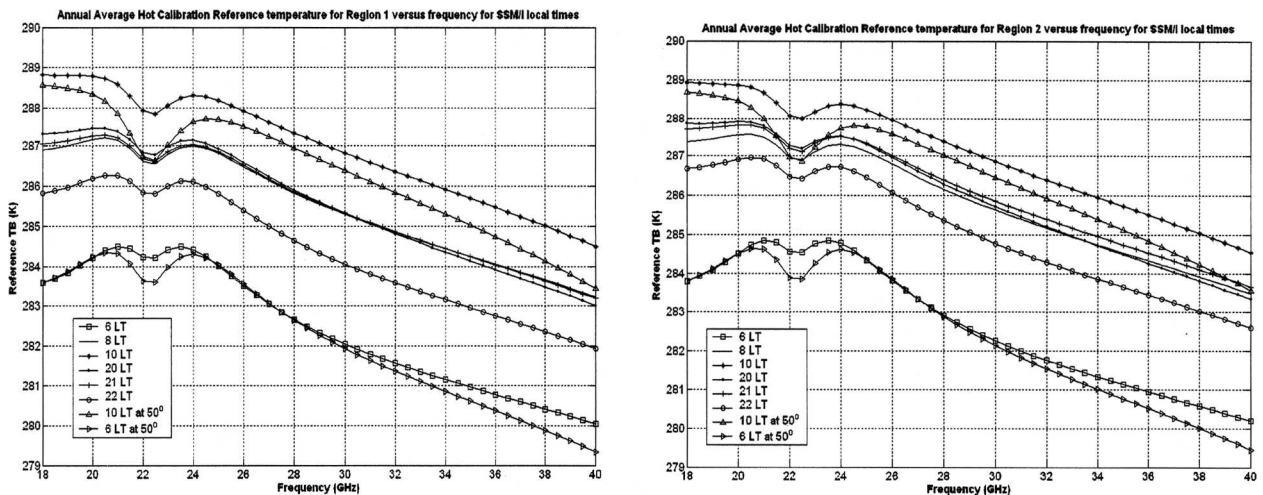


FIG. 4. Reference temperature vs frequency for different SSM/I solar local times:  $T_B$  shown are at nadir incidence except for two 50° incidence cases noted. (left) Region 1 and (right) region 2.

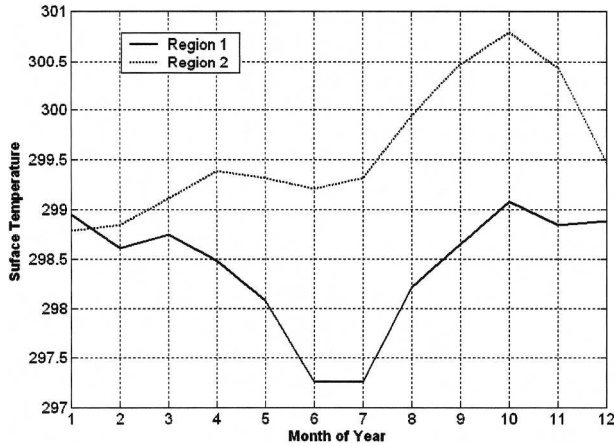


FIG. 5. The climatological surface temperature from observing stations within regions 1 and 2.

ter vapor line where the seasonal variation decreases with increasing incidence. The seasonal variation is greater at 1000 LST compared to 0600 LST. At 1000 LST, the October–July reference temperature difference at a certain frequency is about 3 K, whereas the difference is approximately 1.5 K at 0600 LST. The annual variation at 0600 and 1000 LST is shown in Fig. 7 for 37 GHz.

**5. Application to calibration of microwave radiometers**

The methods described in this study can be used to calibrate satellite microwave radiometers that operate between 18 and 40 GHz and at 0°–55° angles of incidence at the hot end of the  $T_B$  range. There are two approaches for determining the hot reference temperature for a specific frequency, incidence angle, time of day, and time of year. The first approach is to use the

model described in section 3 with SSM/I data. The second approach is to use the empirical reference temperature equation that is derived in section 5b. The first approach is more accurate if the observation times of the radiometer under test match those of SSM/I. That being said, the reference temperature predicted using the first approach with the 0600 LST SSM/I observation should remain applicable in the hours leading up to sunrise. The second approach provides an empirical means to find the reference temperature without the need for any ancillary (SSM/I) data.

*a. Determination of Amazon hot reference temperature from SSM/I observations*

The SSM/I data should be filtered by region and filtered for rain, as described in section 3d. It is recommended that the  $T_B$  data from the radiometer under test also be filtered for rain since our atmospheric model does not account for the effects of rain. Rain-filtering algorithms will differ with instrument. For a single frequency radiometer, filtering can often be accomplished by only using  $T_B$  data within one standard deviation of the mean. For a multifrequency radiometer under test, the  $T_B$  data can be filtered such that data are only used if the difference in  $T_B$  between window channels that are differently affected by rain is within one standard deviation of the mean.

The  $b$  coefficients in Eq. (3) and the upwelling and downwelling effective radiating temperatures must be determined using a radiative transfer model for the frequencies of the radiometer to be calibrated. The coefficients for SSM/I frequencies are included in Table 3, and a plot of the coefficients from 18 to 40 GHz is shown in Fig. 8. A plot of the effective upwelling and downwelling radiating temperatures is shown in Fig. 2. The surface temperature  $T_v$ , atmospheric absorption

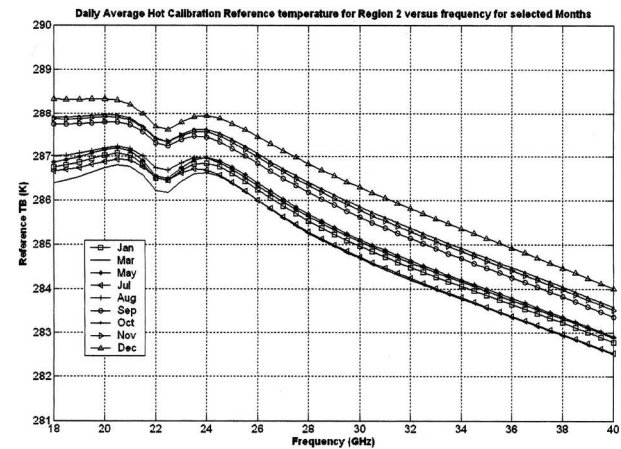
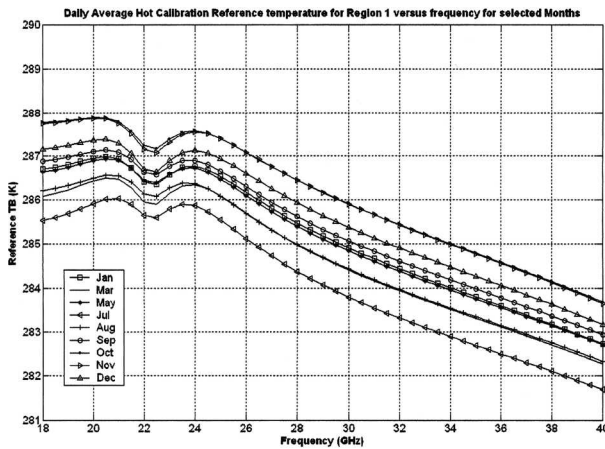


FIG. 6. Daily averaged hot reference temperature vs frequency for various months. (left) Region 1 and (right) region 2.

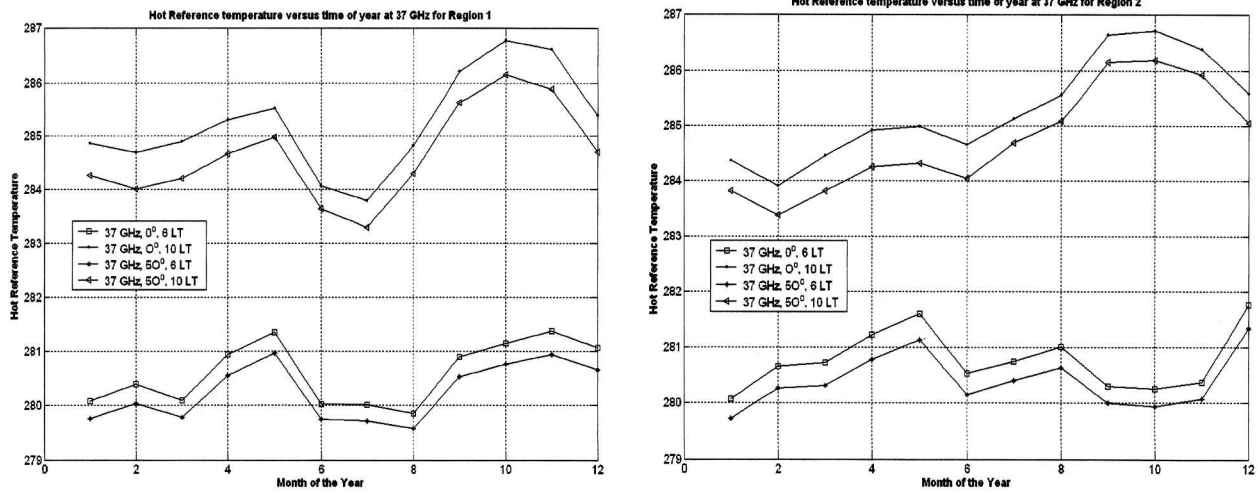


FIG. 7. Annual variation of the hot reference temperature at 37 GHz for 0600 and 1000 LT and  $0^\circ$  and  $50^\circ$  incidence angles for (left) region 1 and (right) region 2. There is little seasonal variation at 0600 LT.

parameter  $A$ , and the single scattering albedo coefficients  $d_0$  and  $d_1$  are determined by solving for them in Eq. (6) using the SSM/I  $T_B$  at 19.35, 22.235, and 37.0 GHz. A nonlinear iterative least squares method can be used to solve for these variables. The average values of  $d_0$  and  $d_1$  are 0.033 and 0.000 53, respectively, over the entire SSM/I dataset used in this study. If these values are used, then only the surface temperature and the atmospheric absorption parameter need to be solved for using the SSM/I  $T_B$ . Once these variables are determined, the reference  $T_B$  for the frequency and angle of incidence of the radiometer under test can be found from the parameterized atmospheric model and Eq. (6).

#### b. Determination of Amazon hot reference temperatures using an empirical formula

Since large datasets of SSM/I  $T_B$  observations are not readily available for some investigators, an em-

pirical formula is derived to estimate the Amazon hot reference  $T_B$  as a function of frequency, incidence angle, time of day, and time of year. The functional dependence of the reference temperature on the four variables is described in section 4, and the empirical model was formulated using this physical basis. A priori information on the sensitivity of the hot reference temperature to each variable was gathered from data used to generate Figs. 3–7. This information was used to set the initial parameterization of the model. A nonlinear, iterative, least squares optimization was used to find the parameters that best fit the data. The model is

$$T_{\text{REF}}(f, \theta, LT, M) = F(f, \theta) + D(LT) + Y(M) + Y(M)DA(LT), \quad (7)$$

where

$$F(f, \theta) = \left( c_1 - c_2 e^{\frac{-(22.235-f)^2}{c_3}} \right) + c_4 f^{-1} + \frac{c_5 \sec \theta}{(f - 22.235)^2 + 0.1} + c_6 e^{\frac{-(f-60.0)^2}{20}} + c_7 f \sec \theta$$

$$D(LT) = \left[ c_8 + c_9 e^{\frac{-(LT-10)^2}{24}} + c_{10} \sin\left(\frac{2\pi LT}{24}\right) \right]$$

$$Y(M) = \left[ c_{11} + c_{12} \sin\left(\frac{2\pi M}{12}\right) + c_{13} \cos\left(\frac{2\pi M}{12}\right) + c_{14} \sin\left(2\left(\frac{2\pi M}{12}\right)\right) + c_{15} \cos\left(2\left(\frac{2\pi M}{12}\right)\right) \right]$$

$$DA(LT) = \left[ c_{16} + c_{17} e^{\frac{-(LT-10)^2}{24}} + c_{18} \sin\left(\frac{2\pi LT}{24}\right) \right],$$

where  $LT$  is local time (1–24),  $M$  is month of the year (integer between 1 and 12),  $\theta$  is angle of incidence (rad), and  $f$  is frequency (GHz). The first term,  $F(f, \theta)$ ,

describes the reference temperature's variation with frequency and incidence angle, accounting for the dip around the water vapor line and the decrease in refer-

TABLE 3. Coefficients in Eq. (3) for the atmospheric model for SSM/I frequencies.

	$b_0$	$b_1$
19.35 GHz	0.0144	0.0217
22.235 GHz	0.0132	0.0658
37.0 GHz	0.0209	0.0215

ence temperature with increasing frequency. The  $D(LT)$  term is the periodic dependence of the reference temperature on local time. The  $Y(M)$  term is the periodic dependence of reference temperature on time of year, and the  $DA(LT)$  term is an amplitude modulation term that is based on local time, which suppresses the seasonal variation in the overnight hours. The  $\exp[-(LT - 10)^2/24]$  term is needed to fit the large change between the 0600 and 1000 LST reference temperature, in part because no SSM/I data fall in the late afternoon hours. The  $\exp[-(f - 60)^2/20]$  term is included because the empirical reference temperatures are observed to be too low around 37.0 GHz without this term. This model is optimized for regions 1 and 2. The coefficients can be found in Tables 4 and 5.

The parameterized empirical model performs very well as compared to the method using the SSM/I data. There is virtually no difference in the reference temperature between the annual average of the empirical model and the annual average of the method using SSM/I data for a given frequency and incidence angle. The rms difference between the empirical formula and the method using the SSM/I data is 0.1 K for both regions for the annual average. The overall rms difference using the empirical relation as compared to the method using SSM/I for a specific time of day (tested at

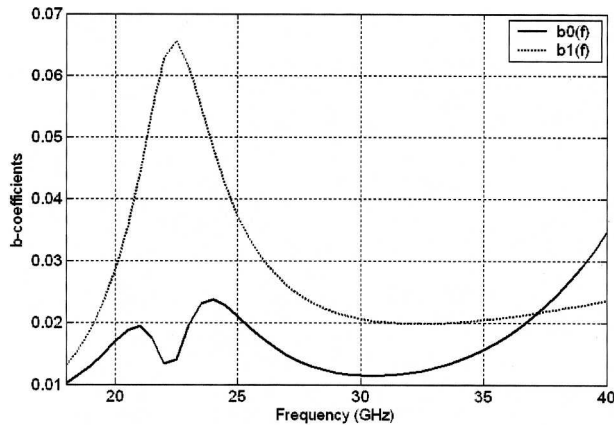


FIG. 8. Spectrum of the coefficients used in Eq. (3) for the atmospheric absorption model. Numeric values at the three SSM/I frequencies are given in Table 3.

TABLE 4. Parameters for the empirical model (7) for region 1.

$c_1$	282.618	$c_7$	-0.215	$c_{13}$	-0.209
$c_2$	-3.214	$c_8$	-2.930	$c_{14}$	-0.116
$c_3$	122.612	$c_9$	4.589	$c_{15}$	-0.432
$c_4$	30.770	$c_{10}$	-2.542	$c_{16}$	-0.353
$c_5$	-0.0848	$c_{11}$	0.926	$c_{17}$	1.216
$c_6$	-0.500	$c_{12}$	0.545	$c_{18}$	-0.302

the SSM/I overpass times) and day of year is 0.6 K. The maximum deviation is less than  $\pm 2$  K. The empirical reference  $T_B$  were able reproduce the daily and annual variations fairly well. Figure 9 shows the empirical annual average reference  $T_B$  versus frequency for the SSM/I local times. This plot can be compared to Fig. 4. Likewise, Figs. 10 and 11, which are equivalent to Figs. 6 and 7, show the empirical reference  $T_B$  dependence on time of year. Caution should be exercised when using the empirical formula for times between 1100 and 1900 LST since there were no SSM/I observations in the database between these times. As a result, the peak of the daytime heating could be underestimated.

*c. Uncertainty of the hot reference temperatures*

The model developed in section 3a is able to fit the SSM/I data at 19.35, 22.235, and 37.0 GHz within the uncertainty of the SSM/I  $T_B$  measurement. Therefore, the uncertainty in the hot reference temperature is due to the extrapolation to other frequencies and incidence angles. The uncertainty in the width of the water vapor absorption line is the most significant error term when extrapolating to other frequencies and is estimated to be approximately 3% (Cruz-Pol et al. 1998). This will contribute less than 0.1 K of uncertainty to the hot reference temperatures that are extrapolated from the  $T_B$ s at the SSM/I frequencies. Another source of uncertainty is how well the surface emission can be modeled by Eq. (2). The assumption in Eq. (2) is that the emission from the canopy is independent of polarization and incidence angle. As a whole, the regions are not completely depolarized, as can be seen in Table 1. There is an average of 0.75- and 0.55-K difference between the  $V$ -pol and  $H$ -pol SSM/I  $T_B$  for regions 1 and 2, respectively. Since the hot reference  $T_B$  were gener-

TABLE 5. As in Table 4 but for region 2.

$c_1$	282.746	$c_7$	-0.215	$c_{13}$	-0.428
$c_2$	-3.199	$c_8$	-2.022	$c_{14}$	0.453
$c_3$	128.738	$c_9$	6.444	$c_{15}$	-0.259
$c_4$	36.793	$c_{10}$	-3.483	$c_{16}$	-0.806
$c_5$	-0.083	$c_{11}$	-0.591	$c_{17}$	2.038
$c_6$	-0.500	$c_{12}$	0.437	$c_{18}$	-1.187

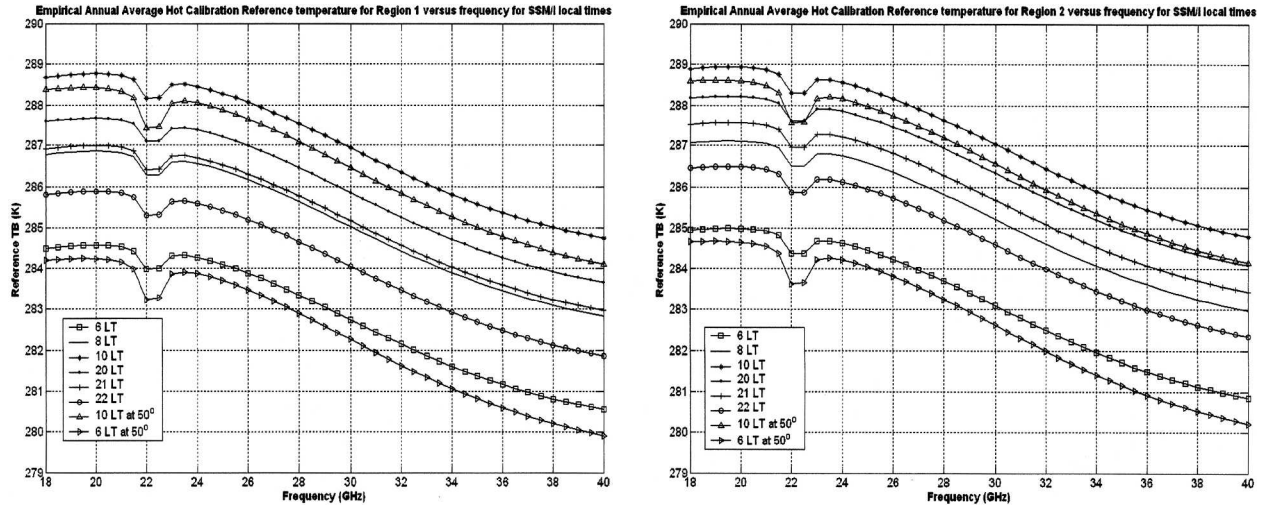


FIG. 9. Empirical reference vs frequency for 0600, 0800, 1000, 1800, 2000, and 2200 LST. These plots represent empirical fits to the observed local time dependence shown in Fig. 4. (left) Region 1; (right) region 2.

ated using the average of the two polarizations, the true  $V$ -pol  $T_B$  at  $53^\circ$  is approximately 0.38 K higher in region 1 and 0.28 K higher in region 2, and the true  $H$ -pol  $T_B$  at  $53^\circ$  is approximately 0.38 K lower in region 1 and 0.28 K lower in region 2. This error term will go to zero at nadir incidence. A simple linear correction that is added to the  $V$ -pol reference  $T_B$  and subtracted from the  $H$ -pol reference  $T_B$  of the form

$$\begin{aligned} e_{\text{REG1}}(\theta) &= 0.0072\theta \\ e_{\text{REG2}}(\theta) &= 0.0053\theta \end{aligned} \quad (8)$$

can be employed to reduce this bias. In Eq. (8),  $\theta$  is in degrees and  $e$  is in kelvin. The standard deviation of the

polarization difference is about 0.8 K; therefore the uncertainty of the hot reference  $T_B$  due to the residual polarized signal is  $0.8/\sqrt{2}$  K. The total uncertainty of the hot reference  $T_B$  derived using the SSM/I data is then the root-sum-square of the line width error term and the polarization error term, which is 0.57 K.

### 6. Conclusions

Accurate brightness temperature calibration for microwave radiometers is essential for the precise retrieval of geophysical parameters. The on-orbit calibration of brightness temperatures can be accomplished by

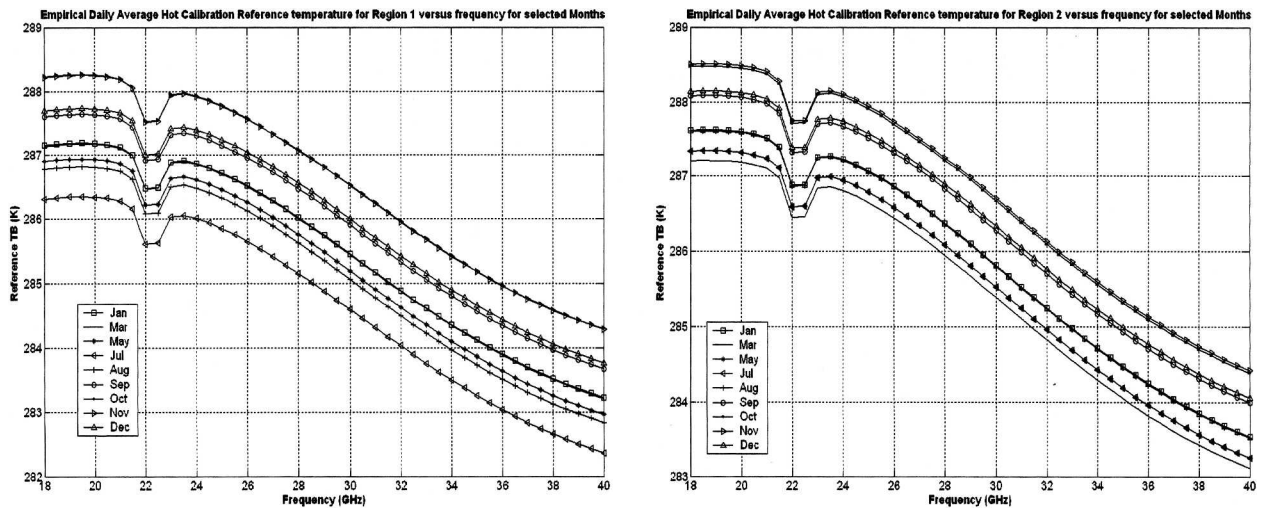


FIG. 10. Empirical reference  $T_B$  vs frequency for selected months. These plots represent empirical fits to the observed annual time dependence shown in Fig. 5. (left) Region 1; (right) region 2.

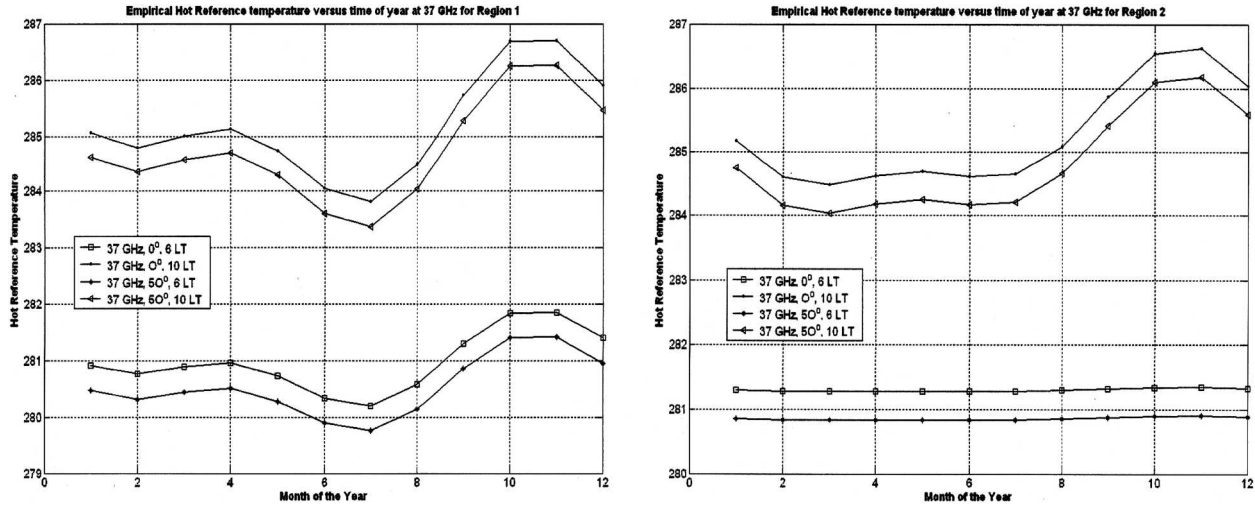


FIG. 11. Empirical reference temperature vs month of year for 0600 and 1000 LST and 0° and 50° incidence. These plots represent empirical fits to the observed annual time dependence shown in Fig. 6. (left) Region 1; (right) region 2.

comparing the  $T_B$  to on-earth reference temperatures at the hot and cold end of the  $T_B$  range. This paper describes a method for determining a hot calibration reference target over the Amazon rain forest. A reference brightness temperature is determined for any radiometer operating between 18 and 40 GHz and between nadir and 55° incidence.

The reference temperature has certain characteristic behaviors as a function of frequency, incidence angle, time of day, and time of year. The reference temperature is largest in October and smallest in July. The amplitude of the seasonal variation is approximately 2.5 K, and the reference temperature has a diurnal variation of about 5.5 K. It is found that the warmest reference temperatures derived from SSM/I data occur at 1000 LST and the coolest at 0600 LST. The amplitude of the seasonal variation is small at 0600 LST. The reference temperature generally decreases from 18 to 40 GHz, with a small depression around the 22.235-GHz water vapor line. There is also a decrease with increasing incidence angle.

The reference temperature can be found in two ways. The first way is to acquire SSM/I data and follow the steps described in section 5a. This will provide an accurate reference temperature for the times of day and year corresponding to the time of the SSM/I data. The second way is to use the empirical expression that is derived in section 5b to find the reference temperature as a function of frequency, incidence angle, hour of the day, and month of year. This function is useful for finding the reference temperature without the need for coincident SSM/I data. The uncertainty of the reference temperature derived using the SSM/I data is estimated

to be 0.57 K. The rms error of the empirical fit to the reference temperatures derived from SSM/I  $T_B$  is 0.6 K for a certain hour of the day and month of the year. The rms error of the empirical model is 0.1 K when averaged over time of day and month of the year. The hot reference temperatures determined in this paper can be used for the on-orbit hot end  $T_B$  calibration of microwave radiometers that are operating at 18–40 GHz and 0°–55° incidence.

REFERENCES

Benoit, A., 1968: Signal attenuation due to neutral oxygen and water vapor, rain and clouds. *Microwave J.*, **11**, 73–80.  
 Colton, M. C., and G. A. Poe, 1999: Intersensor calibration of DMSF SSM/Ts: F-8 to F-14, 1987–1997. *IEEE Trans. Geosci. Remote Sens.*, **37**, 418–439.  
 Cruz Pol, S., C. Ruf, and S. Keihm, 1998: Improved 20–32 GHz atmospheric absorption model. *Radio Sci.*, **22**, 1319–1333.  
 Ferrazzoli, P., and L. Guerriero, 1996: Passive microwave remote sensing of forests: A model investigation. *IEEE Trans. Geosci. Remote Sens.*, **34**, 433–443.  
 Grody, N. C., 1993: Remote sensing of the atmosphere from satellites using microwave radiometry. *Atmospheric Remote Sensing by Microwave Radiometry*, M. A. Janssen, Ed., Wiley, 259–314.  
 Hiltbrunner, D., C. Matzler, and A. Wiesmann, 1994: Monitoring land surfaces with combined DMSP-SSM/I and ERS-1 scatterometer data. *Proc. IEEE Int. Geosci. Remote Sens. Symp.*, Pasadena, CA, IGARSS, 1945–1947.  
 Isaacs, R., Y. Jin, R. Worsham, G. Deblonde, and V. Falcone, 1989: The RADTRAN microwave surface emission models. *IEEE Trans. Geosci. Remote Sens.*, **27**, 433–440.  
 Janssen, M., C. Ruf, and S. Keihm, 1995: TOPEX/Poseidon Microwave Radiometer (TMR): II. Antenna pattern correction and brightness temperature algorithm. *IEEE Trans. Geosci. Remote Sens.*, **33**, 138–146.  
 Keihm, S. J., M. A. Janssen, and C. S. Ruf, 1995: TOPEX/

- Poseidon Microwave Radiometer (TMR): III. Wet troposphere range correction algorithm and pre-launch error budget. *IEEE Trans. Geosci. Remote Sens.*, **33**, 147–161.
- Macelloni, G., S. Paloscia, P. Pampaloni, and R. Ruisi, 2001: Airborne multifrequency L- to Ka-band radiometric measurements over forests. *IEEE Trans. Geosci. Remote Sens.*, **39**, 2507–2513.
- Piepmeyer, J. R., and A. J. Gasiewski, 2001: High-resolution passive polarimetric microwave mapping of ocean surface wind vector fields. *IEEE Trans. Geosci. Remote Sens.*, **39**, 606–622.
- Prigent, C., W. Rossow, and E. Matthews, 1997: Microwave land surface emissivities estimated from SSM/I observations. *J. Geophys. Res.*, **102**, 21 867–21 890.
- Rosenkranz, P., 1993: Absorption of microwaves by atmospheric gases. *Atmospheric Remote Sensing by Microwave Radiometry*, M. A. Janssen, Ed., Wiley, 37–79.
- Ruf, C., S. Keihm, B. Subramanya, and M. Janssen, 1994: TOPEX/POSEIDON microwave radiometer performance and in-flight calibration. *J. Geophys. Res.*, **99** (C12), 24 915–24 926.
- , —, and M. Janssen, 1995: TOPEX/Poseidon Microwave Radiometer (TMR): I. Instrument description and antenna temperature calibration. *IEEE Trans. Geosci. Remote Sens.*, **33**, 125–137.
- Ruf, C. S., 2000: Detection of calibration drifts in spaceborne microwave radiometers using a vicarious cold reference. *IEEE Trans. Geosci. Remote Sens.*, **38**, 44–52.
- Ulaby, F., R. Moore, and A. Fung, 1982: *Microwave Remote Sensing, Active and Passive. Volume II: Radar Remote Sensing and Surface Scattering and Emission Theory*. Artech House, 608 pp.
- , —, and —, 1986: *Microwave Remote Sensing, Active and Passive. Volume III: From Theory to Applications*. Artech House, 1098 pp.
- Walcek, C., and G. Taylor, 1986: A theoretical method for computing vertical distributions of acidity and sulfate production within cumulus clouds. *J. Atmos. Sci.*, **43**, 339–355.
- Wentz, F. J., 1991: User's manual SSM/I antenna temperature tapes. Revision 1, Remote Sensing Systems Tech. Rep. 120191, 9–14.
- Wilheit, T. T., and M. G. Fowler, 1977: Microwave radiometric determination of wind speed at the surface of the ocean during BESEX. *IEEE Trans. Geosci. Remote Sens.*, **25**, 111–120.